

## FEATURE ARTICLE

## Biomimetic Assemblies of Carbon Nanostructures for Photochemical Energy Conversion

Dirk M. Guldi\*

*Institute for Physical Chemistry, Friederich Alexander University—Erlangen—Nuernberg, Egerlandstr. 3, 91058 Erlangen, Germany**Received: February 25, 2005; In Final Form: April 7, 2005*

This feature article summarizes our recent accomplishments in the field of carbon nanostructures, fullerenes and carbon nanotubes, as integrative components in multifunctional hybrid cells that bear large promise for applications as photochemical energy conversion systems.

## 1. Introduction

Currently the construction of multifunctional hybrid cells employable for photoelectrochemical solar energy conversion constitutes one of the most ambitious research objectives of our times. Over the course of the years, the use of inorganic semiconducting materials has dominated the market. However, the production of organic or mixed organic/inorganic solar cells has visibly increased their potential impact to a broad range of innovative technologies. Most promising approaches include dye-sensitized nanocrystalline solar cells,<sup>1</sup> polymer/fullerene blends,<sup>2</sup> small-molecule thin films,<sup>3</sup> and hybrid polymer/nanocrystal devices.<sup>4</sup> Small-area dye-sensitized solar cells have so far reached solar power conversion efficiencies of about 11%,<sup>5</sup> whereas polymer/fullerene heterojunctions and copper phthalocyanine/fullerene hybrid planar/mixed molecular heterojunctions have been reported with 3.5% and 5.7% efficiencies, respectively, under white light illumination.<sup>6</sup> Recently, discotic liquid-crystalline materials have been successfully used in the construction of organic solar cells.<sup>7</sup>

The most frequently encountered problems include topics such as interfacial diffusion of the building blocks (i.e., electron donor and acceptor) and/or lack of efficient light response of large-band-gap semiconductor materials in the visible region.<sup>8</sup> Critical issues in the development of photovoltaic devices include (i) the control over the small- and large-scale organization of donor–acceptor hybrids and (ii) the creation of suitable light and redox gradients. The latter is primarily meant to assist in directing photons and charges in the desired direction.

To match the aforementioned needs, preparing, shaping, and improving multifunctional donor–acceptor hybrids at the molecular scale bears considerable interest.<sup>9,10</sup> It is important that the basic building blocks, which make up these novel hybrids, are readily accessible and tractable. Nanoscale carbon-based materials, fullerenes and carbon nanotubes (CNTs), meet these criteria and, moreover, have emerged as unique materials with tunable physicochemical properties.<sup>11–13</sup> Varying the size, the diameter, and the morphology, for example, of these carbon nanostructures changes band-gap energies, electronic conduction, transport features, etc.

Three-dimensional fullerenes are made of alternating hexagons (i.e., electron rich) and pentagons (i.e., electron deficient)

with diameters starting at 7.8 Å for C<sub>60</sub>.<sup>14</sup> Their extraordinary electron-acceptor properties have resulted in noteworthy advances in the areas of light-induced electron-transfer chemistry and solar energy conversion.<sup>15</sup> It is mainly the small reorganization energy, which fullerenes exhibit in electron-transfer reactions, that is accountable for a particularly noteworthy breakthrough.<sup>16</sup> In particular, ultrafast charge separation together with very slow charge recombination features lead to unprecedented long-lived radical ion pair states formed in high quantum yields.<sup>17</sup>

At least, similar promises rest on quasi-one-dimensional CNTs. CNTs can be thought of as all-hexagon networks of carbon atoms, which have been rolled up to create seamless carbon cylinders.<sup>11</sup> These cylinders reach lengths of centimeters, and each end is, at least theoretically, capped with half of a fullerene moiety.<sup>18</sup> Since the CNT diameter determines the semiconducting band gaps, this parameter is by far the most central one.<sup>19</sup> Specifically, smaller diameters lead to larger band gaps. Single-walled carbon nanotubes (SWNTs) deserve a special mention. They are considered as the fundamental cylindrical structure, since they are the building blocks of both multiwalled carbon nanotubes (MWNTs) and ordered arrays of single-walled carbon nanotubes, also called ropes. The presence of extended, delocalized  $\pi$ -electron systems renders most CNTs very useful for managing charge transfer and charge transport. This and their structural similarity with fullerenes led to the consideration that CNTs should accept electrons readily and transport them with quasi-ballistic features along their tubular axis.<sup>20</sup> In fact, we reported recently on the first intrahybrid electron transfer within a photoexcited SWNT/ferrocene nanohybrid, in which the later constitutes the electron-donor moiety.<sup>20b</sup> No doubt, both nanoscale carbon-based materials, with their unique electron-acceptor characteristics, represent attractive platforms for devising and testing multifunctional hybrid cells.

Organizing nanoscale carbon-based materials with electron-donor components that are dissimilar and sometimes incompatible brings about novel structural features, physical properties, and complex function. These arise from the synergistic interactions of the individual constituents. The excitement about using biological organization principles stems from the ability of biological systems to self-assemble and organize at near-atomic precision into structures with useful and predictable properties.<sup>9,21</sup> In addition, the ability of certain biological systems to

\* Author to whom correspondence should be addressed. E-mail: dirk.guldi@chemie.uni-erlangen.de.

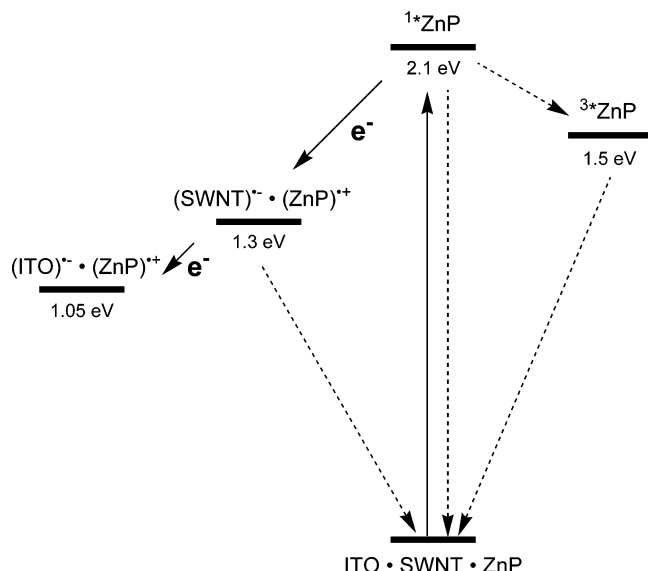


**Figure 1.** Illustration of carbon nanostructures (i.e., SWNTs) and excited-state electron donors (i.e., ZnP) on semiconducting ITO electrodes. Please note that the energy levels depend strongly on the nature of the carbon nanostructures or excited-state electron donors.

handle enormous amounts of data and compute at high speeds should be considered. Biological methods are often more efficient, environmentally friendly, and overall superior to current technology.

The thrust of the ongoing work in our labs is to cross-fertilize biomimetic strategies and materials science to realize multifunctional hybrid cells. More precisely, we pursue the control in the assembly of donor–acceptor hybrids, both in solution and at surfaces, at fundamental length scales and with the precision of natural systems. The biologically inspired organization of molecular receptors (i.e., electron donor) and molecular substrates (i.e., electron acceptor) requires recognition, discrimination, and binding. This, however, can only happen if the binding sites complement each other in size, shape, and chemical functionality. In this context, the simplicity and versatility of electrostatic interactions, augmented by van der Waals forces, provides ample opportunities (i) for probing fundamental/mechanistic aspects and (ii) for optimizing practical/performance aspects.

## 2. Principles to Devise and Control Multifunctional Films

Our approach toward multifunctional hybrid cells focuses on testing semitransparent indium tin oxide (ITO) as an electrode material with conduction band potentials around  $-0.25$  V vs a saturated calomel electrode (SCE). Typically, these ITO electrodes are covered (i) with electron-accepting carbon nanostructures, whose first reduction potentials are in the range between  $-0.5$  and  $-0.7$  V vs SCE, and (ii) with excited-state electron donors, whose excited-state reduction–oxidation potentials are more negative than  $-0.7$  V vs SCE.

To demonstrate the functions of such films, energy diagrams as shown in Figure 1 provide valuable insights. In such diagrams, the energies of the radical ion pair states are correlated with those of the excited precursor states (i.e., singlet and/or triplet). For a system composed of SWNTs and ZnP as the electron acceptor and the electron donor, respectively, we approximate energies of the radical ion pair states—simply from the reduction of SWNTs ( $-0.5$  V vs SCE) and the oxidation of ZnP ( $+0.8$  V vs SCE)—as ca.  $1.3$  eV. The singlet excited-state

energies come from the energy average of the longest wavelength absorption and the shortest wavelength fluorescence. Accordingly, for ZnP the singlet excited-state energy amounts to  $2.1$  eV. The triplet excited state, as directly taken from phosphorescence measurements, is  $1.5$  eV. With all these values in hand we derive driving forces for photoinduced electron-transfer reactions, evolving from the singlet and triplet excited electron donor, that are appreciably large with values around  $0.8$  and  $0.2$  eV, respectively. It is also essential that the subsequent electron shift reaction, that is, electron transfer from the one-electron-reduced acceptor to the conduction band of ITO, is exothermic with driving forces in the range of approximately  $0.25$  eV.

Next, let us reflect on how the molecular building blocks, as they are presented in Figure 2, are deposited onto ITO electrodes to afford multifunctional hybrid cells. Common to all the molecular building blocks is that they are endowed with, at least, one or more ionic headgroups. This renders them, in return, readily soluble/dispensable in aqueous solutions. Such features call for the layer-by-layer technique, which provides great control and flexibility in assembling individual components that are present in aqueous and/or polar media.<sup>22</sup> The key steps of the applied layer-by-layer approach are depicted in Figure 3. These are the electrostatic/van der Waals-driven deposition of a glue (i.e., step I, a polyelectrolyte), of an electron acceptor (i.e., step II, a CNT), and of a chromophore that serves as a photoexcited-state electron donor (i.e., step III, a porphyrin).

Polyelectrolytes are absolutely essential, since in their absence deposition of all the different components (i.e., electron acceptors (step II)/electron donors (step III)) would simply fail. Hydrophobic regions in, for example, poly(diallyl-dimethylammonium) chloride (PDDA<sup>n+</sup>) or sodium poly(styrene-4-sulfonate) (PSS<sup>n-</sup>) ensure their anchoring to the hydrophobic surface. Their hydrophilic headgroups, however, provide multiple point interactions with charged entities via uniformly directed Coulombic forces and short-range van der Waals forces. Both govern physisorption processes between oppositely charged ions (i.e., molecular building blocks in Figure 2). By bringing in electron donors and electron acceptors in consecutive stages of the sequence (i.e., steps II and III), the functionality is established, namely, photoinduced charge separation as the critical step in converting solar light into electrical energy.

Before starting the deposition run, all substrates, quartz slides (i.e., absorption measurements), silicon wafers (i.e., atomic force microscopy (AFM) measurements), and ITO electrodes (i.e., photoconversion measurements), are purified in, for example, piranha solutions for 1 min. Then they are rinsed with deionized water, sonicated for 15 min in water, and once more thoroughly rinsed with deionized water. After this cleaning procedure, the substrates are coated with a polyelectrolyte baselayer by simply immersing them in a 1% aqueous solution of PDDA<sup>n+</sup> at pH 8.5. After 10 min they are retracted from the solution and rinsed with deionized water to remove free PDDA<sup>n+</sup> from the surfaces. After this initial coating step, PDDA<sup>n+</sup> baselayers are exposed for 60 min to a saturated solution of SWNT–PSS<sup>n-</sup> to attach the CNTs and again rinsed with deionized water. The porphyrin is added in the final step of the sequence by dipping the substrates for a period of 60 min into a micromolar aqueous solution of ZnP<sup>8+</sup> (i.e., see Figure 2) and washed with deionized water.

Bearing the nature of Coulombic forces in mind and assuming that each component is homogeneously covered with ionic groups, repulsion between equally charged entities limits each deposition step to monolayer coverage. Independent ellipso-

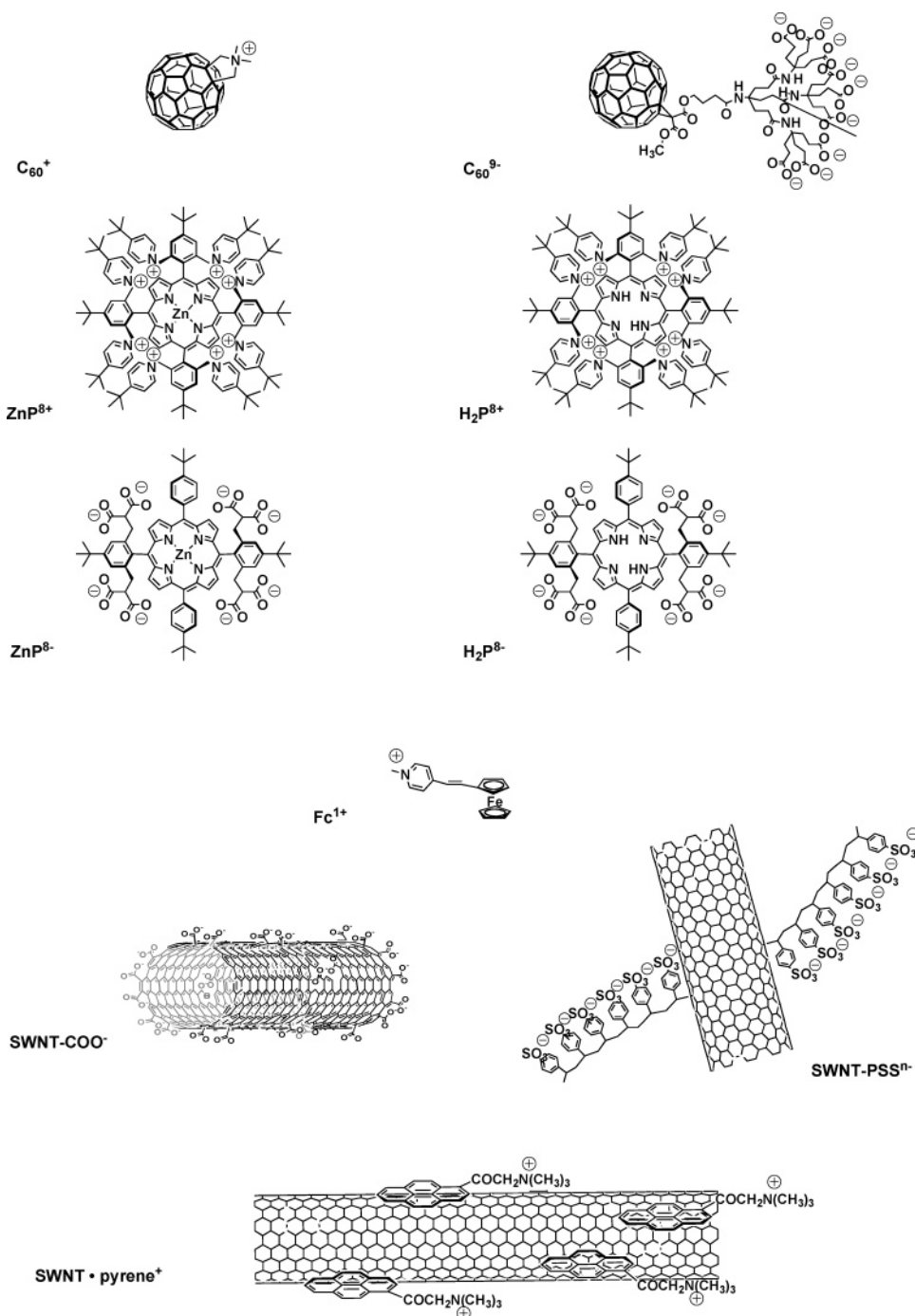


**Figure 2.** Molecular donor and acceptor building blocks considered in this feature article.

metric determination of film thickness corroborated the generality of this assumption.<sup>23</sup> In particular, deposition cycle increments are equal to true monolayers. Generally, absorption cross sections of monolayered films tend to be so weak that sufficiently absorbing electrodes are not attained in a single deposition step. From these experiments, the necessity results to test 20 and sometimes even more individual coating runs (vide supra).

The versatility, flexibility, broadness, and benefits that lie in our approach are apparent when taking into account that (i) densely packed surfaces can be fabricated in each layer, (ii) individual components can be replaced, (iii) the sequence can be repeated, (iv) the sequence can be altered, and (v) environmentally stable and robust surfaces can be constructed. Control over these factors is vital to achieve structural uniformity,

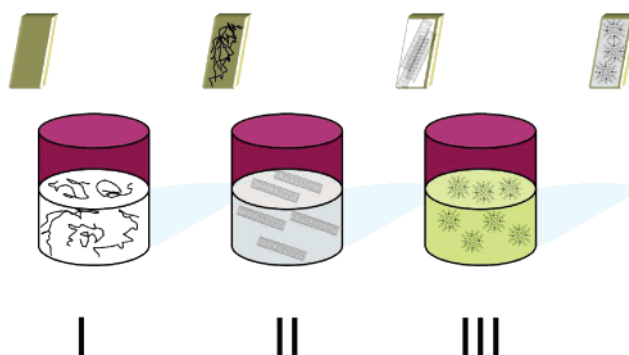


**Figure 3.** Principles of the layer-by-layer deposition technique, illustrated for the deposition of polyelectrolytes (i.e., step I), CNTs (i.e., step II), and porphyrins (i.e., step III).



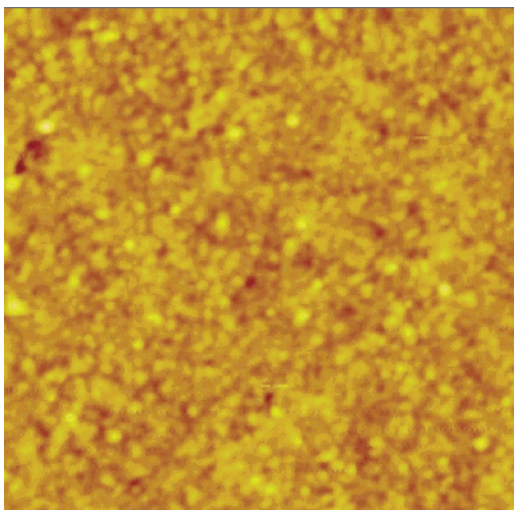


**Figure 4.** AFM image of a single  $C_{60}^+$  layer on a silicon wafer. The image size is  $1\ \mu\text{m} \times 1\ \mu\text{m}$ .

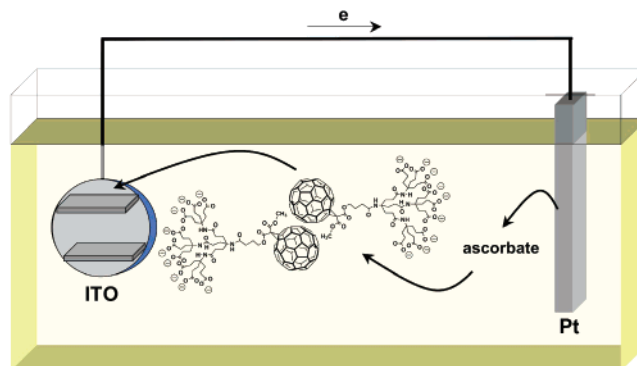
integrity, functionality, and composition at the molecular level en route toward multifunctional electrode surfaces.

### 3. Fullerenes

In the first part of this section, two different fullerene derivatives,  $C_{60}^{9-}$  and  $C_{60}^+$  (i.e., see Figure 2), as electron acceptors are discussed.<sup>24,25</sup>  $C_{60}^{9-}$  and  $C_{60}^+$  were deposited (i.e., step II) onto oppositely charged PDDA<sup>n+</sup> and PSS<sup>n-</sup>, respectively.<sup>23,26</sup> Hereby optical absorption spectroscopy emerged as a convenient means to confirm the presence of  $C_{60}^{9-}$  and  $C_{60}^+$ . In particular, characteristic peaks developed at 226, 260, and 336 nm, which are somewhat broader than those seen in condensed media. This stands in sharp contrast to the polyelectrolyte layers that exhibit transitions that are mainly located in the UV region below 200 nm. Spectrophotometry was further complemented by atomic force microscopy; see Figure 4. While PDDA<sup>n+</sup> and PSS<sup>n-</sup> form fairly flat surfaces with occasional pores, after adsorption of  $C_{60}^{9-}$  and  $C_{60}^+$ , the roughness of the surface decreases markedly. Now we realize that the surface becomes uniformly covered with characteristic 20–50 nm two-dimensional  $C_{60}$  crystals. These crystals amalgamate into a continuous uniform film. Once the  $C_{60}^{9-}$  and  $C_{60}^+$  monolayers are absorbed, strong van der Waals interactions between individual  $C_{60}$  cores facilitate bilayer formation, leaving the ionic groups sticking out from the surface.

Immediately after their preparation, multifunctional hybrid cells are immersed into ascorbate solutions with a Pt cathode connected externally to the ITO anode to measure the photocurrents. When the cells are illuminated with visible light, distinct photocurrent patterns develop. Insights into the photoactivity of  $C_{60}^{9-}$  and  $C_{60}^+$  doublelayers, which are deposited onto ITO electrodes, namely, hole versus electron transport, were gathered upon adding variable concentrations of methyl viologen, electron acceptors, or ascorbic acid, electron donors, to the electrolyte solution. Two different tendencies were noted when exciting with visible light. For methyl viologen, a concentration-dependent decrease in the photocurrent was noted. Circumstances are generated in which the electron acceptor competes with ITO to accept electrons from the photoexcited  $C_{60}^{9-}$  or  $C_{60}^+$  double layers. In contrast, when ascorbic acid is present a net increase of the photocurrent resulted. A maximum response is observed at 1 mM, while at higher quencher concentrations though, the currents do not increase further. These trends suggest that the electron transfer into the ITO conduction

### SCHEME 1: Schematic Illustration of Photocurrent Generation in ITO Electrodes Covered with a Single $C_{60}^{9-}$ Stack<sup>a</sup>



<sup>a</sup> Blue indicates the base layer of polyelectrolyte deposited initially onto ITO.

band evolves mainly from the one-electron-reduced state of  $C_{60}^{9-}$  or  $C_{60}^+$  with some smaller contributions from their photoexcited states (Scheme 1). It is important to note that the earlier mechanism requires excited-state electron-transfer quenching (i.e., ascorbic acid) and, hence, competes with excited-state annihilation processes or alternative deactivation channels.

While the photoaction spectra confirm unequivocally the photosensitizing features of the  $C_{60}^{9-}$  or  $C_{60}^+$  double layers in the visible region, a quantitative analysis discloses a rather low monochromatic incident photon to current conversion efficiency (IPCE) of only 0.01%.<sup>26</sup> Still this value constitutes a 10-fold increase, relative to bare PDDA<sup>n+</sup>, which lacks any photo- and redox activity at all under the same experimental conditions. The generally weak absorption cross sections of these films are further augmented by the fact that major  $C_{60}$  absorptions are only in the 200–400 nm range with extinction coefficients as high as  $100\,000\ \text{M}^{-1}\ \text{cm}^{-1}$  and as low as  $2000\ \text{M}^{-1}\ \text{cm}^{-1}$ .<sup>27</sup> But in our photocurrent measurements, we typically cut out light below 375 nm to avoid direct excitation across the ITO band gap. In the 400–700 nm range, the  $C_{60}$  extinction coefficients are well below  $2000\ \text{M}^{-1}\ \text{cm}^{-1}$ .

In an attempt to overcome the inherently weak absorptions, we started to cover ITO electrodes with stacks of, for example,  $C_{60}^+$  double layers and PSS<sup>n-</sup> monolayers.<sup>23</sup> To illustrate this with the example given in Figure 3, the stacking approach implies the repetition of step I (i.e., PSS<sup>n-</sup>) and step II (i.e.,  $C_{60}^+$ ). From absorption spectra of the deposited films on quartz, repeatable  $C_{60}^+$  absorption patterns are deduced that translate into linear dependencies for up to 20 individual stacks. Both factors are meaningful criteria that demonstrate the satisfactory and uniform stacking of individually deposited films, namely, PSS<sup>n-</sup> monolayers and  $C_{60}^+$  double layers. AFM of subsequent  $C_{60}^+$  double layers did not change appreciably from what is described above for the first double layer; see Figure 4. However, when analyzing the photocurrents as a function of layers, a truly linear increase in photocurrent is only seen up to a limited number of sandwich layers (i.e., maximum response around 3 or 4 stacks). Implicit is the lack of long-range electronic coupling with the electron-collecting electrode material, due to (i) increasing distance and (ii) the insulating nature of the polyelectrolyte layers (i.e., PSS<sup>n-</sup>).

### 4. Fullerenes and Excited-State Electron Donors: Porphyrins

The above results necessitate the integration of an excited-state electron donor into multifunctional hybrid cells rather than

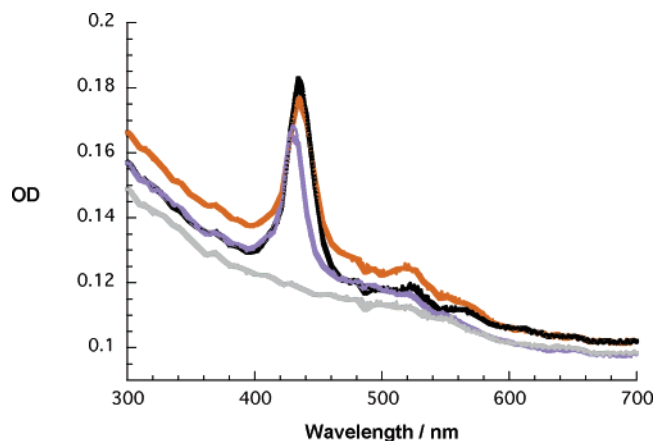


**Figure 5.** UV-vis absorption spectra of a quartz substrate (bearing monolayer coverages of  $C_{60}^{9-}$  (gray line),  $C_{60}^{9-}/H_2P^{8+}$  (purple line),  $C_{60}^{9-}/H_2P^{8+}/ZnP^{8-}$  (black line), and  $C_{60}^{9-}/H_2P^{8+}/ZnP^{8-}/Fc^{1+}$  (orange line) as electro- and photoactive components).

fullerene double layer stacking. This is expected to improve two major design principles: (i) enhancing the absorption cross section in the visible part of the solar spectrum, where even twenty  $C_{60}^{+}$  doublelayers absorb rather weakly and (ii) ensuring a rapid electron transfer or transduction of excited-state energy to avoid annihilation processes or other energy losses. Among the many feasible approaches, the two following choices will be discussed in detail: (i) depositing donors and acceptors that are not covalently linked to each other in two separate steps or (ii) depositing covalently linked donor-acceptor arrays in one single step.

Let us first direct our attention to the first scenario, namely, carrying out step II (i.e.,  $C_{60}^{9-}$ ) and step III (i.e.,  $ZnP^{8+}$  or  $H_2P^{8+}$ ) of the sequence outlined in Figure 3.<sup>26,28</sup> Ensembles in which  $ZnP^{8+}$  or  $H_2P^{8+}$  building blocks are integrated show much stronger responses throughout the visible spectrum. In particular, in Figure 5 both Soret regions, centered around 425 nm, and Q-band regions, centered around 575 nm, clearly identify the porphyrinic chromophores as the major photoactive species. Considering the size of the  $C_{60}$  crystals (i.e., 20–50 nm) in the first bilayer, our failure to detect AFM-resolved  $ZnP^{8+}$  or  $H_2P^{8+}$  molecules is in line with the expectation. The only detectable difference between just  $C_{60}^{9-}$  and  $C_{60}^{9-}/ZnP^{8+}$  or  $C_{60}^{9-}/H_2P^{8+}$  is an appreciable increase in the surface roughness. Relative to  $C_{60}^{9-}$ , the monochromatic IPCE values for  $H_2P^{8+}$ -containing (0.08%) and  $ZnP^{8+}$ -containing (0.15%) systems reflect a 7- and 13-fold amplification, respectively; see Figure 6. The higher activity, seen in the later case, is due to more exothermic electron-transfer thermodynamics in the  $C_{60}^{9-}/ZnP^{8+}$  couple, as seen numerous times for charge-separation dynamics of similar donor-acceptor systems in condensed media.<sup>15</sup>

If the deposition order of the components is reversed, that is, essentially performing step III before step II, then the efficiency decreases.<sup>23</sup> In particular,  $H_2P^{8+}/C_{60}^{9-}$  gives rise to a 5-fold drop in the photocurrent relative to  $C_{60}^{9-}/H_2P^{8+}$ . This is rationalized on the basis that a mismatch in the individual redox steps is generated. For instance, instead of an electron injection, which evolves from the one-electron-reduced  $C_{60}^{9-}$  into the ITO conduction band, the photocurrent mechanism changes to hole injection from the one-electron-oxidized  $H_2P^{8+}$  to ITO. An electrical bias was applied to either accelerate or decelerate the charge injection (i.e., electron or hole) into ITO. In the case of  $C_{60}^{9-}/H_2P^{8+}$ , going from +200 to -400 mV, a gradual photocurrent decrease of up to 54% is noted. Such a decrease implies that through fine-tuning the electrical bias the

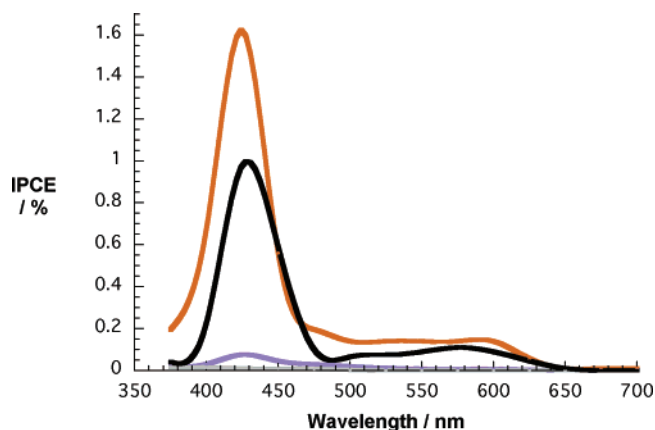
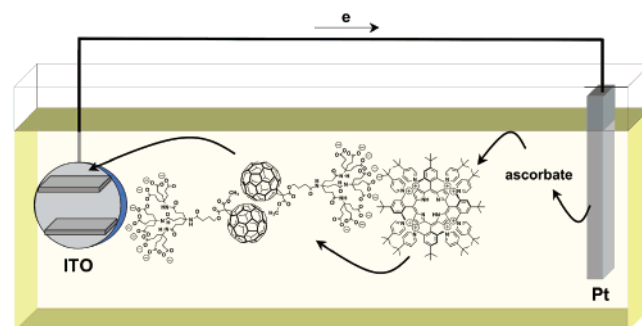


**Figure 6.** Photoaction spectrum of photoactive ITO electrodes covered with  $C_{60}^{9-}$  (gray line),  $C_{60}^{9-}/H_2P^{8+}$  (purple line),  $C_{60}^{9-}/H_2P^{8+}/ZnP^{8-}$  (black line), and  $C_{60}^{9-}/H_2P^{8+}/ZnP^{8-}/Fc^{1+}$  (orange line) as electro- and photoactive components under deoxygenated and short circuit conditions.

## SCHEME 2: Schematic Illustration of Photocurrent Generation in ITO Electrodes Covered with a Single $C_{60}^{9-}/H_2P^{8+}$ Stack<sup>a</sup>



<sup>a</sup> Blue indicates the base layer of polyelectrolyte deposited initially onto ITO.

energy gap for  $C_{60}^{9-} \rightarrow ITO$  is reduced and the charge flow is suppressed. For  $H_2P^{8+}/C_{60}^{9-}$ , 35% higher photocurrents are generated, suggesting that  $H_2P^{8+} \rightarrow ITO$  becomes more and more exothermic. In tests with aerobic and anaerobic conditions, we only noted differences for  $H_2P^{8+}/C_{60}^{9-}$ , which resulted in a loss of photocurrent that maximizes at ~20%. In conclusion, charge separation from the photoexcited porphyrin to  $C_{60}^{9-}$  generates electron-hole pairs. While the energetic position of the ITO conduction band favors a thermodynamically driven electron transfer from the one-electron-reduced  $C_{60}^{9-}$ , the sacrificial electron donor sodium ascorbate reduces the one-electron-oxidized porphyrins. Scheme 2 provides an illustration of the major reactions.

To follow up on the second option, we employed two sets of covalently linked  $C_{60}$ -porphyrin classes, which were assembled in a single procedure, step II.<sup>29,30</sup> Class I, denoted as  $C_{60}-ZnP^-$  and  $C_{60}-H_2P^-$ , carry carboxylic groups at one of the porphyrin's phenyl groups, while in class II,  $C_{60}^+-H_2P$  and  $C_{60}^+-NiP$ , ammonium groups are attached to the fullerene termini of the linear arrays. For both classes, it holds true that spectrophotometry discloses all of the fullerene and porphyrin signatures in the UV and visible spectra and that AFM helps to visualize 20–50 nm crystals on the surface. Despite these similarities, depending to which end the ionic functionality is attached to (i.e., fullerene vs porphyrin, see Figure 7) entirely different photocurrent scenarios are created (vide infra).

For class I, electrostatic linkage of the  $C_{60}-ZnP^-$  and  $C_{60}-H_2P^-$  arrays to the ITO electrode places the primary electron

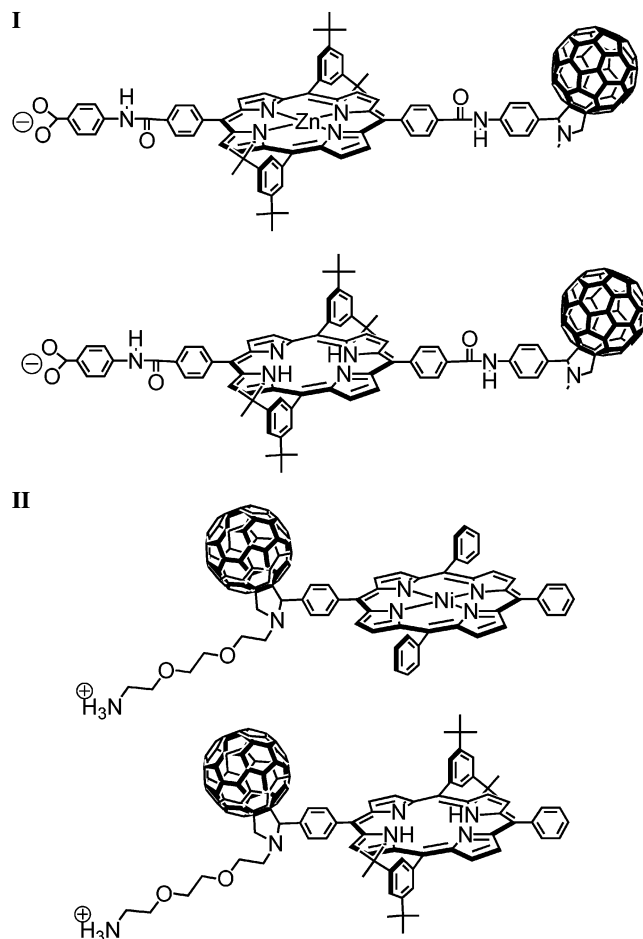


**Figure 7.** Structure of class I (i.e.,  $C_{60}-ZnP^-$  and  $C_{60}-H_2P^-$ ) and class II (i.e.,  $C_{60}^+-H_2P$  and  $C_{60}^+-NiP$ ) donor-acceptor arrays.

donors adjacent to the ITO electrode, while the electron acceptor sits in a remote position relative to the ITO electrode.<sup>29</sup> Thus, within the context of photocurrent generation the following charge-transfer scenario develops. Initial charge separation within the  $C_{60}-ZnP^-$  and  $C_{60}-H_2P^-$  arrays is followed by hole injection into the ITO electrode. Applying a negative bias at the ITO electrode surface is expected to facilitate the hole injection from the one-electron-oxidized electron donor. Accordingly, changing the bias from +200 to 0 mV and to -200 mV vs Ag/AgCl increases the photocurrent 1.5 and 1.8 times, respectively.

Generally, photocurrents under monochromatic light illumination of  $C_{60}-H_2P^-$  (IPCE 0.12%) are stronger by a factor of 2 to 3.3, depending on the electrolyte composition, than those recorded for  $C_{60}-ZnP^-$  (IPCE 0.04%). This efficiency difference is understood based on the energetics of the generated radical ion pair; the one-electron-oxidized  $H_2P^+$  is thermodynamically more reactive than the oxidized analogue of  $ZnP^+$ .

For class II, applying a positive bias (i.e., +200 mV) at the ITO electrode leads in the absence of oxygen for  $C_{60}^+-NiP$  to a 20% amplification of the photocurrent, due to a facilitated electron transfer to ITO.<sup>30</sup> Conversely, under oxygenated conditions the photocurrents decreased by 10%, which is due to the competition between the biased electrode and  $O_2$  in their electron-transfer reaction with the one-electron-reduced fullerene. Further support for this hypothesis comes from the fact that applying a negative bias (i.e., -200 mV) increased the photocurrent overall for the oxygenated sample by up to 30%.

We would like to reemphasize that linking donor-acceptor arrays of classes I and II to the polyelectrolytes creates

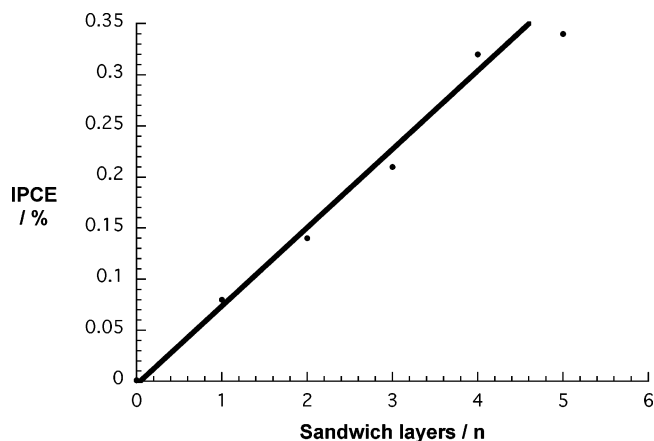


**Figure 8.** Plot of IPCE as a function of the deposited layers of  $C_{60}^{9-}/H_2P^{8+}$ .

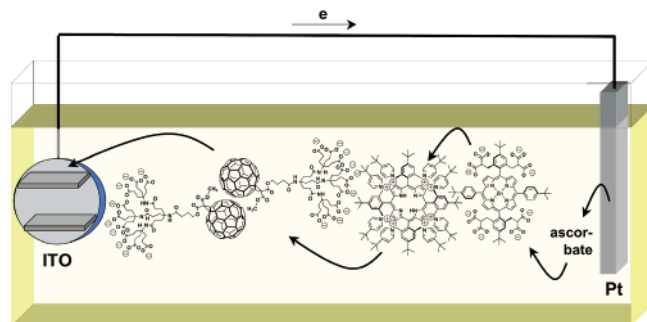
predominantly hydrophobic surfaces. This is mainly due to the presence of fullerene and/or porphyrin moieties. Associative forces such as van der Waals interactions, as they typically govern the connection between individual fullerene and porphyrin entities, are then believed to be the driving forces for the one-dimensional controlled buildup of subsequent monolayers onto these predominantly hydrophobic surfaces. Considering such scenarios for the case of  $C_{60}^+-NiP$ ,  $PSS^{n-}$  easily self-assembles and, subsequently, opens the way for repeating steps I (i.e.,  $PSS^{n-}$ ) and II (i.e.,  $C_{60}^+-NiP$ ). The sequential layering was repeated successfully up to 20 times. However, as far as the photocurrent response is concerned, only slight increases were seen, which were mainly limited to the first and second layers, while beyond that point the currents remained virtually unchanged. Overall, the increase is very moderate with values in the range of 5–10%. Again, the increasing distance and insulating nature of the polyelectrolyte layers are believed to be responsible for the lack of appreciable amplification (vide supra).

More success in maximizing the absorption cross section and, at the same time, enhancing the photocurrent performance was accomplished in building up  $C_{60}^{9-}/H_2P^{8+}$  or  $C_{60}^{9-}/ZnP^{8+}$  stacks, namely, repeating steps II and III.<sup>31</sup> Please note that in this workup method no insulating layers of polyelectrolytes (i.e.,  $PSS^{n-}$ ) are embedded. Ten stacks of, for example,  $C_{60}^{9-}/H_2P^{8+}$  led to absorbencies of around 0.6 at the Soret-band maximum, relative to 0.08 for a single stack. Figure 8 documents that the IPCE grows linearly, up to four stacks before leveling off, with a maximum value of 0.35% at five stacks. Stacking  $C_{60}^{9-}/ZnP^{8+}$  gives rise to a similar behavior and reaches a maximum IPCE of 0.38%.

## 5. Constructing Gradients

From the above considerations, several criteria emerged that, if implemented, should enable meaningful photocurrent generation: (i) avoiding photochemical annihilation processes, (ii) eliminating insulating layers, (iii) funneling the absorbed light, and (iv) directing the charge flow. To meet all of these criteria, we mimicked our recent results on covalently linked  $C_{60}-H_2P-ZnP$ ,  $C_{60}-H_2P-ZnP-Fc$ , and  $C_{60}-ZnP-ZnP-Fc$  linear arrays.<sup>32</sup> Here well-tuned redox gradients are beneficial, through a cascade of short-range electron-transfer steps, to separate charges in the final radical ion pairs over distances of up to ca. 50 Å. Inspired by this finding, we took the aforementioned  $C_{60}^{9-}/H_2P^{8+}$  and  $C_{60}^{9-}/ZnP^{8+}$  systems and covered both of them with a single layer of  $ZnP^{8-}$  (Scheme 3).<sup>23</sup> Absorption spectra



**SCHEME 3: Schematic Illustration of Photocurrent Generation in ITO Electrodes Covered with a Single  $C_{60}^{9-}/H_2P^{8+}/ZnP^{8-}$  Stack<sup>a</sup>**


<sup>a</sup> Blue indicates the base layer of polyelectrolyte deposited initially onto ITO.

in Figure 5 serve as spectroscopic evidence for the successful deposition. As a result of the  $ZnP^{8-}$  presence, we see the monochromatic IPCEs increasing from 0.15% (i.e.,  $C_{60}^{9-}/ZnP^{8+}$ ) to 0.3% (i.e.,  $C_{60}^{9-}/ZnP^{8+}/ZnP^{8-}$ ) and from 0.08% (i.e.,  $C_{60}^{9-}/H_2P^{8+}$ ) to 1.0% (i.e.,  $C_{60}^{9-}/H_2P^{8+}/ZnP^{8-}$ ). Considering the nearly 13-fold increase in the latter case, the following three parameters alter the reactivity. First, the new  $ZnP^{8-}$  building block further enhances the absorption coverage of the solar spectrum. Second, it passes on its excited-state energy unidirectionally to  $H_2P^{8+}$  or  $C_{60}^{9-}$ . Third, once the radical ion pair is formed, the electrons and holes shift into different directions; while ITO still collects the electrons, the holes transfer to  $ZnP^{8-}$ .

When adding additional layers of  $ZnP^{8+}$  or  $ZnP^{8-}$  to  $C_{60}^{9-}/H_2P^{8+}/ZnP^{8-}$ , the currents continue to increase to 1.15% (i.e., three layers) and 1.35% (i.e., five layers).<sup>31</sup> Obviously, the photons that are absorbed by the light-harvesting  $ZnP^{8+}/ZnP^{8-}$  are trapped efficiently by  $H_2P^{8+}$ . Different is the trend when using  $C_{60}^{9-}/ZnP^{8+}/ZnP^{8-}$ . Here the currents drop linearly to 0.16%, for example, when six layers are present. Obviously, photons are being absorbed and filtered by the top layers. This contribution is, however, lost for the overall photocurrent generation.

Ultimately,  $Fc^+$  was added to create  $C_{60}^{9-}/H_2P^{8+}/ZnP^{8-}/Fc^{1+}$ .<sup>23</sup> Comparing now this more complex system with the simpler  $C_{60}^{9-}/H_2P^{8+}$  and  $C_{60}^{9-}/H_2P^{8+}/ZnP^{8-}$ , we see a 20- and 1.6-fold enhancement of the photocurrent, respectively. This corresponds to a high monochromatic IPCE value of 1.6%.

In these new multifunctional hybrid cells, multipurpose energy/redox gradients within a series of chromophores are essential in helping (i) to attain good absorption coverage of the solar spectrum, (ii) to funnel solar light unidirectionally to an active core, (iii) to separate charges within that active core, and (iv) to transport electrons and holes into opposite directions.

## 6. Carbon Nanotubes

In the case of SWNTs, very different challenges emerged. Typically, bundles of SWNT are intractable and, therefore, impossible to deposit. Early on we pursued a concept in which we utilized oxidatively treated samples,  $SWNT-COO^-$  (i.e., samples that underwent refluxing in  $HNO_3$  or  $H_2SO_4$  supplemented by excessive and lengthy ultrasonication), that have 5% of the total number of carbon atoms as  $COOH$  functionalities.<sup>33</sup> In fact, moderate success was achieved through this  $SWNT-COO^-$  approach. But such drastic conditions in processing CNTs bring about major changes in the  $\pi$ -electronic structure and, subsequently, in the properties of CNTs. Please note that

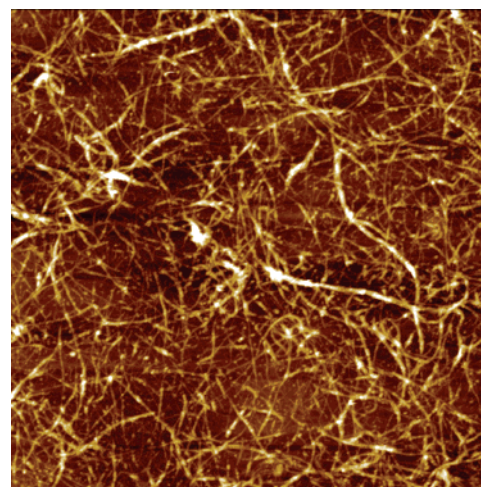


**Figure 9.** AFM image of a single  $SWNT/pyrene^+$  layer on a silicon wafer. The image size is  $5\ \mu m \times 5\ \mu m$ .

photocurrent measurements were never carried out with these strongly altered  $SWNT-COO^-$  materials.

A major breakthrough/refinement in depositing SWNTs came with the supramolecular treatment of CNTs with amphiphilic pyrene derivatives that carry ionic side chains (i.e., 1-(trimethylammonium acetyl)) as hydrophilic parts.<sup>34</sup> We developed a workup procedure that allows enrichment of SWNTs in aqueous media.<sup>20f</sup> Consequently, we were able to accomplish the electrostatically driven deposition of  $SWNT/pyrene^+$  associates onto polyelectrolyte surfaces. This would correspond to step II in Figure 3. Again, absorption spectroscopy with quartz substrates and atomic force microscopy with silicon wafers are both suitable for obtaining structural insights. On quartz substrates,  $PDDA^{n+}$  and  $PSS^{n-}$  exhibit transitions that are mainly located in the UV region below 200 and 260 nm, respectively. SWNTs, however, are strong UV-vis-near-IR absorbers, since the van Hove singularities extend up to 1500 nm.<sup>35</sup> Also the strong  $\pi-\pi^*$  transitions of  $pyrene^+$  can be observed at 235, 290, and 365 nm. Figure 9 shows randomly organized bundles of SWNTs on a pretreated silicon wafer for the case of  $SWNT/pyrene^+$ .

Similar results were found for water-soluble SWNTs that are grafted with poly(sodium 4-styrenesulfonate) ( $SWNT-PSS^{n-}$ ).<sup>20d,36</sup> Notable in  $SWNT-PSS^{n-}$ , the number of functional groups is significantly reduced relative to what was estimated for  $SWNT-COO^-$ , but overall the number is definitely higher than that in  $SWNT/pyrene^+$ . In fact, several analysis techniques were used to evaluate a  $SWNT$  to  $PSS^{n-}$  ratio of 55:45.

In photoelectrochemical cells that just contain  $SWNT/pyrene^+$  or  $SWNT-PSS^{n-}$ , a mechanistic picture evolves that is essentially identical with that described for  $C_{60}^{9-}$  or  $C_{60}^{+}$ , analogous to that shown in Scheme 1.<sup>37</sup> For  $SWNT/pyrene^+$ , in good agreement with the absorption spectra, a photoaction spectrum (Figure 10) showed maximum light response at 375 nm, combined with a relatively low monochromatic IPCE of about 0.1% in the presence of 1 mM ascorbate. Although the conditions are slightly different relative to  $C_{60}^{9-}$  or  $C_{60}^{+}$ , 0.1 M  $Na_3PO_4$  vs 0.1 M  $Na_2HPO_4$ , the efficiency is nevertheless appreciably enhanced.

## 7. Carbon Nanotubes and Excited-State Electron Donors: Porphyrins

Similar to the situation explored for fullerenes, the help of a visible-light chromophore is needed, especially to photosensitize

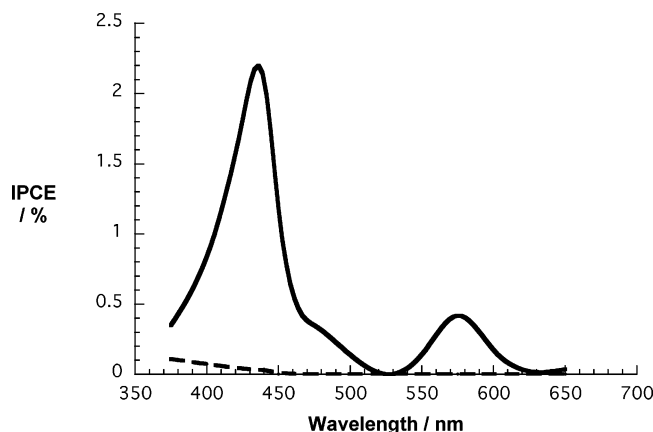
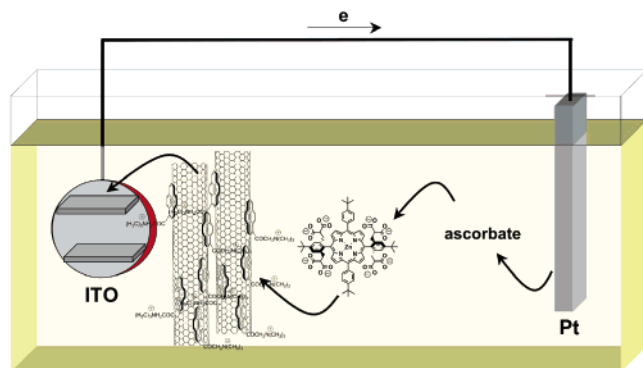


**Figure 10.** Photoaction spectrum of a single SWNT/pyrene<sup>+</sup> (dashed line) and a single SWNT/pyrene<sup>+</sup>/ZnP<sup>8-</sup> stack (full line): 0.1 M Na<sub>3</sub>PO<sub>4</sub>, 1 mM sodium ascorbate, N<sub>2</sub> purged, no electrochemical bias.

**SCHEME 4: Schematic Illustration of Photocurrent Generation in ITO Electrodes Covered with a Single SWNT/Pyrene<sup>+</sup>/ZnP<sup>8-</sup> Stack<sup>a</sup>**



<sup>a</sup> Red indicates the base layer of polyelectrolyte deposited initially onto ITO.

the charge transfer from the reduced SWNTs into the electron-collecting ITO electrode. This led us to test ZnP<sup>8-</sup>.<sup>37</sup>

Photoaction and photocurrent measurements with different sets of electrodes were performed in aqueous solutions containing 0.1 M Na<sub>3</sub>PO<sub>4</sub>. First, photoaction spectra with monochromatic light were recorded, which confirm the photoactivity of the porphyrin chromophores. Next, in photocurrent measurements, in which the entire solar spectrum was used, we probed mechanistic aspects. Upon addition of sodium ascorbate, an electron donor that restores the oxidized porphyrins, the photocurrents of the system increased markedly. Obviously, regeneration of the initial porphyrin state helps to close the photoelectrochemical circuit. Scheme 4 illustrates a summary of the individual steps that take place for SWNT/pyrene<sup>+</sup>/ZnP<sup>8-</sup>. In analogy to what is seen in solution experiments, photoexcitation of the porphyrin chromophores is succeeded by the formation of radical ion pairs, namely, reduced SWNT and oxidized ZnP<sup>8+</sup>. The electrons flow exothermically from the reduced acceptor to the ITO conduction band, while the oxidized donors are reduced at the solid–liquid interface by ascorbate.

Relative to bare ITO electrodes (i.e., <0.001%) and those that are covered with only SWNT/pyrene<sup>+</sup> (i.e., 0.1%), the amplifications seen in the IPCEs were significant. Without biasing the ITO electrode, a SWNT/pyrene<sup>+</sup>/ZnP<sup>8-</sup> cell gave rise to a promising 1.8% IPCE. This represents a nearly 20-fold increase. With a positive bias, which is meant to facilitate the electron collection at the ITO conduction band, an additional doubling of the photocurrents was achieved.

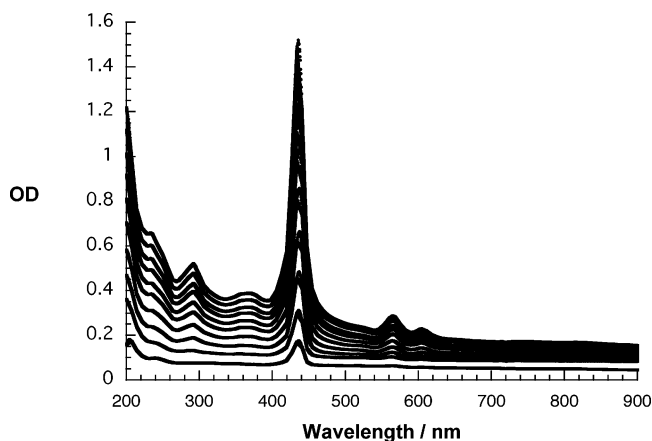


**Figure 11.** Absorption spectra of variable (i.e., up to 10) SWNT/pyrene<sup>+</sup>/ZnP<sup>8-</sup> stacks on quartz.

Repetition of the deposition steps (i.e., step II, SWNT/pyrene<sup>+</sup>, and step III, ZnP<sup>8-</sup>) allows the modification of the polyelectrolyte baselayers with SWNT/pyrene<sup>+</sup>/ZnP<sup>8-</sup> stacks. The repetitive growth is followed through absorption spectroscopy, of which a representative example is shown in Figure 11. The transitions of pyrene<sup>+</sup> (i.e., 235, 290, and 365 nm), ZnP<sup>8-</sup> (i.e., 435, 565, and 605 nm) and SWNTs (i.e., 685, 745, 815, and 880 nm) grow linearly up to 10 stacks, that is, 10 alternating layers of SWNT/pyrene<sup>+</sup> and ZnP<sup>8-</sup>. Interestingly, we see in these 10 stacks an overall increase in photocurrent generation. Largely enhanced absorption cross sections favor the photocurrent increase. In addition, strong electronic coupling between the stacks, which is augmented by the intriguing SWNT transport features within the individual layers, is believed to be critical for the observed trends. Translating the currents into monochromatic IPCEs, maximum values for SWNT/pyrene<sup>+</sup>/ZnP<sup>8-</sup> amount to 4.2%. With a +200 mV bias, the corresponding monochromatic IPCE is ~8.5% at the absorption peak of ZnP<sup>8-</sup>. Although many more than 10 stacks were deposited, the photocurrents stagnate and/or drop beyond this point.

All of the films that were investigated responded promptly and uniformly to “light on” and “light off” intervals. Importantly, for SWNT/pyrene<sup>+</sup>/ZnP<sup>8-</sup> exceptionally reproducible and stable photocurrents were obtained.

## 8. Conclusions and Outlook

In summary, combining carbon nanostructures, fullerenes and carbon nanotubes, with electron-donor groups represents an innovative concept to solar-energy-harvesting systems, which leads to appreciable conversion of solar light into practical electricity. The chromophores absorb visible photons, electron–hole pairs are formed at the donor–acceptor interface, the reduced carbon nanostructures transfer an electron to the ITO, and ascorbate reduces the oxidized electron donor. So far, the highest monochromatic internal photoconversion efficiencies were obtained with SWNT/pyrene<sup>+</sup>/ZnP<sup>8-</sup> cells that give rise to values of up to ~8.5%. Please note that these conditions do not resemble completely the solar power conversion efficiencies with reference solar spectral irradiance at an air mass 1.5.<sup>38</sup>

The photocurrents are quite high for the first attempts with new donor–acceptor pairs. It is reasonable to ascribe the limitations seen in the photocurrents to (i) the efficiency of electron–hole separation at the donor–acceptor interface or (ii) the efficiency of the transfer of electrons from the electron acceptor to the electron-collecting ITO electrode. Moreover, the efficiency of electron–hole separation might depend either on



the inherent energy levels of the donor and the acceptor or on the number and distance of contacts between the donor and the acceptor. Without doubt, another key variable is the state of aggregation of the SWNT. It is safe to assume that individual tubes and bundles of different sizes may all exhibit different behaviors. Also, the metallic character of some SWNTs must be considered, since they give rise to much smaller band gaps than what is typically seen for semiconducting SWNTs. Among semiconducting tubes, narrow diameter SWNTs might have a higher-energy conduction band that correlates with inherently lower conductivity. These are some of the most interesting directions in which the field of "carbon nanostructures for solar energy conversion" must develop if the myriad of expectations should ever become reality.

In terms of devising efficient solar energy conversion systems, the versatile use of nanoscale carbon-based materials, especially that of fullerenes, as key components in polymer/fullerene blends and self-assembled monolayers on gold or ITO electrodes should be highlighted.<sup>39–41</sup> In this connection, the covalent grafting of fullerene moieties to conjugated polymer backbones revealed a promising approach to prepare solar cell active layers in which both electronic and morphological properties could be controlled at once.<sup>42</sup>

**Acknowledgment.** This work was carried out with partial support from the European Union (RTN network "WONDER-FULL"), Deutsche Forschungsgemeinschaft (SFB 583), FCI, and the Office of Basic Energy Sciences of the U. S. Department of Energy. This is document NDRL-4604 from the Notre Dame Radiation Laboratory. I am deeply indebted to Professors Ford, Fukuzumi, Hirsch, Imahori, Jux, Kotov, Maggini, Martin, Prato, Valli, and Zilbermann for their productive collaborations and numerous stimulating discussions.

## References and Notes

- (1) (a) Lewis, N. S. *Nature* **1983**, *305*, 671. (b) Oregan, B.; Graetzel, M. *Nature* **1991**, *353*, 737. (c) Graetzel, M. *Nature* **2001**, *414*, 338.
- (2) (a) Sariciftci, N. S.; Smilowitz, L.; Heeger, A. J.; Wudl, F. *Science* **1992**, *258*, 1474. (b) Yu, G.; Gao, J.; Hummelen, J. C.; Wudl, F.; Heeger, A. J. *Science* **1995**, *270*, 1789. (c) Brabec, C. J.; Sariciftci, N. S.; Hummelen, J. C. *Adv. Funct. Mater.* **2001**, *11*, 15.
- (3) (a) Shah, A.; Torres, P.; Tscharnner, R.; Wyrsh, N.; Keppner, H. *Science* **1999**, *285*, 692. (b) Peumans, P.; Uchida, S.; Forrest, S. R. *Nature* **2003**, *425*, 158.
- (4) (a) Halls, J. J. M.; Walsh, C. A.; Greenham, N. C.; Marseglia, E. A.; Friend, R. H.; Moratti, S. C.; Holmes, A. B. *Nature* **1995**, *376*, 498. (b) Katz, H. E.; Lovinger, A. J.; Johnson, J.; Kloc, C.; Siegrist, T.; Li, W.; Lin, Y. Y.; Dodabalapur, A. *Nature* **2000**, *404*, 478. (c) Nelson, J. *Science* **2001**, *293*, 1059. (d) Huynh, W. U.; Dittmer, J. J.; Alivisatos, A. P. *Science* **2002**, *295*, 2425.
- (5) Kern, R.; Van Der Burg, N.; Chmiel, G.; Ferber, J.; Hasenhiindl, G.; Hirsch, A.; Kinderman, R.; Kroon, J.; Meyer, A.; Meyer, T.; Niepmann, R.; Van Roosmalen, J.; Schill, C.; Sommeling, P.; Spath, M.; Uhlendorf, I. *Opto-Electron. Rev.* **2000**, *8*, 284.
- (6) (a) Padinger, F.; Rittberger, R. S.; Sariciftci, N. S. *Adv. Funct. Mater.* **2003**, *13*, 85. (b) Xue, J.; Uchida, S.; Rand, B. P.; Forrest, S. R. *Appl. Phys. Lett.* **2004**, *85*, 5757.
- (7) Schmidt-Mende, L.; Fechtenkötter, A.; Müllen, K.; Moons, E.; Friend, R. H.; MacKenzie, J. D. *Science* **2001**, *293*, 1119.
- (8) (a) Fendler, J. H.; Dekany, I. *Nanoparticles in Solids and Solutions*; Kluwer: Dordrecht, 1996. (b) Kamat, P. V.; Meisel, D. *Semiconductor Nanoclusters*; Elsevier: Amsterdam, 1997. (c) Fendler, J. H. *Nanoparticle and Nanostructured Films*; Wiley-VCH: Weinheim, 1998. (d) Kamat, P. V. *Chem. Rev.* **1993**, *93*, 267. (e) Hagfeldt, A.; Grätzel, M. *Chem. Rev.* **1995**, *95*, 49.
- (9) (a) Vögtle, F. *Supramolecular Chemistry*; Wiley: Chichester, 1991. (b) Lehn, J. M. *Supramolecular Chemistry—Concepts and Perspectives*; VCH: Weinheim, 1995. (c) Steed, J. W.; Atwood, J. L. *Supramolecular Chemistry*; Wiley: Chichester, 2000. (d) *Comprehensive Supramolecular Chemistry*; Atwood, J. L.; Davies, J. E. D.; MacNicol, D. D.; Vögtle, F.; Lehn, J.-M., Eds.; Pergamon/Elsevier: Oxford, 1996; Vols. 1–10. (e) Lindoy, L. F.; Atkinson, I. M. *Self-Assembly in Supramolecular Systems*; Royal Society of Chemistry: Cambridge, 2000.
- (10) *Introduction to Nanotechnology*; Poole, C. P., Owens, F. J., Eds.; Wiley-Interscience: Weinheim, 2003.
- (11) (a) Harris, P. *Carbon Nanotubes and Related Structures: New Materials for the Twenty-First Century*; Cambridge University Press: Cambridge, 2001. (b) *Carbon Nanotubes: Synthesis, Structure, Properties and Applications*; Dresselhaus, M. S., Dresselhaus, G., Avouris, P., Eds.; Springer: Berlin, 2001. (c) Reich, S.; Thomsen, C.; Maultzsch, J. *Carbon Nanotubes: Basic Concepts and Physical Properties*; VCH: Weinheim, 2004.
- (12) Special Issue on Carbon Nanotubes. *Acc. Chem. Res.* **2002**, *35*, 997.
- (13) (a) *Lecture Notes on Fullerenes Chemistry*; Taylor, R., Ed.; Imperial College Press: London, 1999. (b) *Fullerenes and Related Structures*; Topics in Current Chemistry 199; Hirsch, A., Ed.; Springer: Berlin, 1999. (c) *Fullerenes: From Synthesis to Optoelectronic Properties*; Guldi, D. M., Martin, N., Eds.; Kluwer Academic Publishers: Dordrecht, 2002.
- (14) (a) Kroto, H. W. *Nature* **1987**, *329*, 529. (b) Krätschmer, W.; Lamb, L. D.; Fostiropoulos, K.; Huffman, D. R. *Nature* **1990**, *347*, 354. (c) Haddon, R. C.; Brus, L. E.; Raghavachari, K. *Chem. Phys. Lett.* **1986**, *131*, 165. (d) Morton, J. R.; Negri, F.; Preston, K. F. *Acc. Chem. Res.* **1998**, *31*, 63. (e) Rosseinsky, M. J. *J. Mater. Chem.* **1995**, *5*, 1497. (f) Weaver, J. H. *Acc. Chem. Res.* **1992**, *25*, 143.
- (15) (a) Imahori, H.; Sakata, Y. *Adv. Mater.* **1997**, *9*, 537. (b) Prato, M. *J. Mater. Chem.* **1997**, *7*, 1097. (c) Martin, N.; Sanchez, L.; Illescas, B.; Perez, I. *Chem. Rev.* **1998**, *98*, 2527. (d) Imahori, H.; Sakata, Y. *Eur. J. Org. Chem.* **1999**, 2445. (e) Diederich, F.; Gomez-Lopez, M. *Chem. Soc. Rev.* **1999**, *28*, 263. (f) Guldi, D. M. *Chem. Commun.* **2000**, 321. (g) Reed, C. A.; Bolskar, R. D. *Chem. Rev.* **2000**, *100*, 1075. (h) Gust, D.; Moore, T. A.; Moore, A. L. *J. Photochem. Photobiol., B* **2000**, *58*, 63. (i) Gust, D.; Moore, T. A.; Moore, A. L. *Acc. Chem. Res.* **2001**, *34*, 40. (j) Guldi, D. M.; Martin, N. *J. Mater. Chem.* **2002**, *12*, 1978–1992. (k) Guldi, D. M. *Chem. Soc. Rev.* **2002**, *31*, 22. (l) Imahori, H.; Mori, Y.; Matano, Y. *J. Photochem. Photobiol., C* **2003**, *4*, 51. (m) Nierengarten, J. F. *Top. Curr. Chem.* **2003**, *228*, 87. (n) Guldi, D. M. *Pure Appl. Chem.* **2003**, *75*, 1069. (o) El-Khouly, M. E.; Ito, O.; D'Souza, F. J. *Photochem. Photobiol., C* **2004**, *5*, 79. (p) Guldi, D. M.; Prato, M. *Chem. Commun.* **2004**, 2517. (q) Segura, J. L.; Martin, N.; Guldi, D. M. *Chem. Soc. Rev.* **2005**, *34*, 31.
- (16) (a) Imahori, H.; Hagiwara, K.; Akiyama, T.; Akoi, M.; Taniguchi, S.; Okada, T.; Shirakawa, M.; Sakata, Y. *Chem. Lett.* **1996**, 263, 545. (b) Guldi, D. M.; Asmus, K.-D. *J. Am. Chem. Soc.* **1997**, *119*, 5744.
- (17) Imahori, H.; Yamada, H.; Guldi, D. M.; Endo, Y.; Shimomura, A.; Kundu, S.; Yamada, K.; Okada, T.; Sakata, Y.; Fukuzumi, S. *Angew. Chem., Int. Ed.* **2002**, *41*, 2344.
- (18) Zhu, H. W.; Xu, C. L.; Wu, D. H.; Wei, B. Q.; Vajtai, R.; Ajayan, P. M. *Science* **2002**, *296*, 884.
- (19) (a) O'Connell, M. J.; Bachilo, S. M.; Huffman, C. B.; Moore, V. C.; Strano, M. S.; Haroz, E. H.; Rialon, K. L.; Boul, P. J.; Noon, W. H.; Kittrell, C.; Ma, J.; Hauge, R. H.; Weisman, R. B.; Smalley, R. E. *Science* **2002**, *297*, 593. (b) Bachilo, S. M.; Strano, M. S.; Kittrell, C.; Hauge, R. H.; Smalley, R. E.; Weisman, R. B. *Science* **2002**, *298*, 2361.
- (20) (a) Georgakilas, V.; Kordatos, K.; Prato, M.; Guldi, D. M.; Holzinger, M.; Hirsch, A. J. *Am. Chem. Soc.* **2002**, *124*, 760. (b) Guldi, D. M.; Marcaccio, M.; Paolucci, D.; Paolucci, F.; Tagmatarchis, N.; Tasis, D.; Vázquez, E.; Prato, M. *Angew. Chem., Int. Ed.* **2003**, *42*, 4206. (c) Melle-Franco, M.; Marcaccio, M.; Paolucci, D.; Paolucci, F.; Georgakilas, V.; Guldi, D. M.; Prato, M.; Zerbetto, F. *J. Am. Chem. Soc.* **2004**, *126*, 1646. (d) Guldi, D. M.; Rahman, G. N. A.; Ramey, J.; Marcaccio, M.; Paolucci, D.; Paolucci, F.; Qin, S. H.; Ford, W. T.; Balbinot, D.; Jux, N.; Tagmatarchis, N.; Prato, M. *Chem. Commun.* **2004**, 2034. (f) Guldi, D. M.; Rahman, G. M. A.; Jux, N.; Tagmatarchis, N.; Prato, M. *Angew. Chem., Int. Ed.* **2004**, *43*, 5526. (g) Alvaro, M.; Atienzar, P.; de la Cruz, P.; Delgado, J. L.; Garcia, H.; Langa, F. J. *Phys. Chem. B* **2004**, *108*, 12691. (h) Sheeney-Hai-ichia, L.; Basnar, B.; Willner, I. *Angew. Chem., Int. Ed.* **2005**, *44*, 78. (i) Guldi, D. M.; Taieb, H.; Rahman, G. M. A.; Tagmatarchis, N.; Prato, M. *Adv. Mater.* **2005**, *17*, 871. (j) Guldi, D. M.; Rahman, G. M. A.; Jux, N.; Balbinot, D.; Tagmatarchis, N.; Prato, M. *Chem. Commun.* **2005**, 2038.
- (21) (a) McDermott, G.; Priece, S. M.; Freer, A. A.; Hawthornthwaite-Lawless, A. M.; Papiz, M. Z.; Cogdell, R. J.; Isaacs, N. W. *Nature* **1995**, *374*, 517. (b) Barber, J. *Nature* **1988**, *333*, 114. (c) *Supramolecular Chemistry*; NATO ASI Series, Series C 371; Balzani, V., de Cola, L., Eds.; Kluwer Academic Publishers: Dordrecht, 1992.
- (22) (a) Decher G.; Hong, J. D. *Ber. Bunsen-Ges. Phys. Chem.* **1991**, *95*, 1430. (b) Ferreira, M.; Cheung, J. H.; Rubner, M. F. *Thin Solid Films* **1994**, *244*, 806. (c) Keller, S. W.; Kim, H. N.; Mallouk, T. E. *J. Am. Chem. Soc.* **1994**, *116*, 8817. (d) Lvov, Y.; Decher, G.; Haas, H.; Mohwald, H.; Kalachev, A. *Physica B* **1994**, *198*, 89. (e) Kotov, N. A. *Nanostruct. Mater.* **1999**, *12*, 789. (f) Dubas, S. T.; Schlenoff, J. B. *Macromolecules* **1999**, *32*, 8153. (g) Hammond, P. T. *Cur. Opin. Colloid Interface Sci.* **2000**, *4*, 430. (h) Durstock, M. F.; Taylor, B.; Spry, R. J.; Chiang, L.; Reulbach, S.; Heitfeld, K.; Baur, J. W. *Synth. Met.* **2001**, *116*. (i) Ferreira, M.; Rubner, M. F.; Hsieh, B. R. *Mater. Res. Soc. Symp. Proc.* **1994**, *328*, 119. (j) Yoo, S.; Shiratori, S. S.; Rubner, M. F. *Macromolecules* **1998**, *31*, 4309.

- (23) Luo, C.; Guldi, D. M.; Maggini, M.; Menna, E.; Mondini, S.; Kotov, N. A.; Prato, M. *Angew. Chem., Int. Ed.* **2000**, *39*, 3905.
- (24) (a) Balbinot, D.; Atalick, S.; Guldi, D. M.; Hatzimarinaki, M.; Hirsch, A.; Jux, N. *J. Phys. Chem. B* **2003**, *107*, 13273. (b) Braun, M.; Atalick, S.; Guldi, D. M.; Lanig, H.; Brettreich, M.; Burghardt, S.; Hatzimarinaki, M.; Ravanelli, E.; van Eldik, R.; Hirsch, A. *Chem.—Eur. J.* **2003**, *9*, 3867.
- (25) (a) Guldi, D. M.; Zilbermann, I.; Anderson, G. A.; Kotov, N. A.; Prato, M. *J. Am. Chem. Soc.* **2004**, *126*, 14340. (b) Guldi, D. M.; Zilbermann, I.; Anderson, G.; Kotov, N. A.; Tagmatarchis, N.; Prato, M. *J. Mater. Chem.* **2005**, *15*, 114.
- (26) Guldi, D. M.; Zilbermann, I.; Anderson, G.; Li, A.; Balbinot, D.; Jux, N.; Hatzimarinaki, M.; Hirsch, A.; Prato, M. *Chem. Commun.* **2004**, 726.
- (27) Guldi, D. M.; Prato, M. *Acc. Chem. Res.* **2000**, *33*, 695.
- (28) Guldi, D. M.; Zilbermann, I.; Lin, A.; Braun, M.; Hirsch, A. *Chem. Commun.* **2004**, 96.
- (29) Zilbermann, I.; Anderson, G. A.; Guldi, D. M.; Yamada, H.; Imahori, H.; Fukuzumi, S. *J. Porphyrins Phthalocyanines* **2003**, *7*, 357.
- (30) (a) Guldi, D. M.; Pellarini, F.; Prato, M.; Granito, C.; Troisi, L. *Nano Lett.* **2002**, *2*, 965. (b) Guldi, D. M.; Zilbermann, I.; Anderson, G. A.; Kordatos, K.; Prato, M.; Tafuro, R.; Valli, L. *J. Mater. Chem.* **2004**, *14*, 303.
- (31) Unpublished results.
- (32) (a) Imahori, H.; Guldi, D. M.; Tamaki, K.; Yoshida, Y.; Luo, C.; Sakata, Y.; Fukuzumi, S. *J. Am. Chem. Soc.* **2001**, *123*, 6617. (b) Guldi, D. M.; Imahori, H.; Tamaki, K.; Kashiwagi, Y.; Yamada, H.; Sakata, Y.; Fukuzumi, S. *J. Phys. Chem.* **2004**, *108*, 541.
- (33) (a) Guldi, D. M.; Holzinger, M.; Hirsch, A.; Georgakilas, V.; Prato, M. *Chem. Commun.* **2003**, 1130. (b) Mamedov, A. A.; Kotov, N. A.; Prato, M.; Guldi, D. M.; Wicksted, J. P.; Hirsch, A. *Nat. Mater.* **2002**, *1*, 190.
- (34) Nakashima, N.; Tomonari, Y.; Murakami, H. *Chem. Lett.* **2002**, 638.
- (35) Strano, M. S.; Dyke, C. A.; Usrey, M. L.; Barone, P. W.; Allen, M. J.; Shan, H.; Kittrell, C.; Hauge, R. H.; Tour, J. M.; Smalley, R. E. *Science* **2003**, *301*, 1519.
- (36) Qin, S. H.; Qin, D. Q.; Ford, W. T.; Resasco, D. E.; Herrera, J. E. *Macromolecules* **2004**, *37*, 752.
- (37) Guldi, D. M.; Rahman, G. M. A.; Jux, N.; Prato, M.; Qin, S.; Ford, W. T. *Angew. Chem., Int. Ed.* **2005**, *44*, 2015.
- (38) Rostalski, J.; Meissner, D. *Sol. Energy Mater. Sol. Cells* **2000**, *61*, 87.
- (39) (a) Hasobe, T.; Kashiwagi, Y.; Absalom, M. A.; Sly, J.; Hosomizu, K.; Crossley, M. J.; Imahori, H.; Kamat, P. V.; Fukuzumi, S. *Adv. Mater.* **2004**, *16*, 975. (b) Yamada, H.; Imahori, H.; Nishimura, Y.; Yamazaki, I.; Fukuzumi, S. *Adv. Mater.* **2002**, *14*, 892. (c) Imahori, H.; Fukuzumi, S. *Adv. Mater.* **2001**, *13*, 1197. (d) Hasobe, T.; Imahori, H.; Kamat, P. V.; Ahn, T. K.; Kim, S. K.; Kim, D.; Fujimoto, A.; Hirakawa, T.; Fukuzumi, S. *J. Am. Chem. Soc.* **2005**, *127*, 1216. (e) Hasobe, T.; Kamat, P. V.; Absalom, M. A.; Kashiwagi, Y.; Sly, J.; Crossley, M. J.; Hosomizu, K.; Imahori, H.; Fukuzumi, S. *J. Phys. Chem. B* **2004**, *108*, 12865. (f) Hasobe, T.; Imahori, H.; Kamat, P. V.; Fukuzumi, S. *J. Am. Chem. Soc.* **2003**, *125*, 14962.
- (40) (a) Yang, X.; van Duren, J. K. J.; Janssen, R. A. J.; Michels, M. A. J.; Loos, J. *Macromolecules* **2004**, *37*, 2151. (b) Wurthner, F.; Chen, Z.; Hoeben, F. J. M.; Osswald, P.; You, C.-C.; Jonkheijm, P.; Herrikhuyzen, J. v.; Schenning, A. P. H. J.; van der Schoot, P. P. A. M.; Meijer, E. W.; Beckers, E. H. A.; Meskers, S. C. J.; Janssen, R. A. J. *J. Am. Chem. Soc.* **2004**, *126*, 10611. (c) van Duren, J. K. J.; Yang, X.; Loos, J.; Bulle-Lieuwma, C. W. T.; Sieval, A. B.; Hummelen, J. C.; Janssen, R. A. J. *Adv. Funct. Mater.* **2004**, *14*, 425. (d) Mihailitchi, V. D.; van Duren, J. K. J.; Blom, P. W. M.; Hummelen, J. C.; Janssen, R. A. J.; Kroon, J. M.; Rispens, M. T.; Verhees, W. J. H.; Wienk, M. M. *Adv. Funct. Mater.* **2003**, *13*, 43. (e) Janssen, R. A. J.; Jansen, J. F. G. A.; van Haare, J. A. E. H.; Meijer, E. W. *Adv. Mater.* **1996**, *8*, 494. (f) Wienk, M. M.; Kroon, J. M.; Verhees, W. J. H.; Knol, J.; Hummelen, J. C.; van Hal, P. A.; Janssen, R. A. J. *Angew. Chem., Int. Ed.* **2003**, *42*, 3371. (g) Yang, X.; Loos, J.; Veenstra, S. C.; Verhees, W. J. H.; Wienk, M. M.; Kroon, J. M.; Michels, M. A. J.; Janssen, R. A. J. *Nano. Lett.* **2005**, *5*, 579.
- (41) (a) Kymakis, E.; Amaratunga, G. A. J. *Appl. Phys. Lett.* **2002**, *80*, 112. (b) Kymakis, E.; Amaratunga, G. A. J. *Sol. Energy Mater. Sol. Cells* **2003**, *80*, 465. (c) Yang, C.; Wohlgenannt, M.; Vardeny, Z. V.; Blau, W. J.; Dalton, A. B.; Baughman, R.; Zakhidov, A. A. *Physica B* **2003**, *338*, 366.
- (42) Cravino, A.; Sariciftci, N. S. *J. Mater. Chem.* **2002**, *12*, 1931.